Journal of Energy Storage 98 (2024) 113047

Contents lists available at ScienceDirect

Journal of Energy Storage

journal homepage: www.elsevier.com/locate/est

Research papers

Yolk–shell vanadium pentoxide integrated electrode for high-performance stretchable lithium metal battery

Muthu Gnana Theresa Nathan [a], Seon-Young Yeon [a], Jae Seob Lee [b], Min Su Jo [b], Gil Chan Hwang [c], Hong-Il Kim [a], Fanglin Wu [d,*], Guk-Tae Kim [a], Ying Liu [a], Jin-Hee Kim [e], Jung Sang Cho [b,f,*], Jae-Kwang Kim [a,*]

[a] Department of Energy Convergence Engineering, Cheongju University, 258 Daeseong-ro, Cheongju, Chungbuk 28503, Republic of Korea
[b] Department of Engineering Chemistry, Chungbuk National University, Chungbuk 28644, Republic of Korea
[c] Department of Earth System Sciences, Yonsei University, Seoul 03722, Republic of Korea
[d] State Key Laboratory of Advanced Technology for Materials Synthesis and Processing, Wuhan University of Technology, Wuhan 430070, China
[e] Department of Biomedical Laboratory Science, College of Health Science Cheongju University, Cheongju, Chungbuk 28503, Republic of Korea
[f] Biomedical Research Institute, Chungbuk National University Hospital, Chungbuk 361-763, 28644, Republic of Korea

ARTICLE INFO

Keywords:
Structure transform
Yolk–shell V_2O_5@PEO
Integrated electrodes
Zig-Zag truncated lithium metal
Stretchable lithium metal batteries

ABSTRACT

Vanadium pentoxide (V_2O_5) stands out as a preferred cathode material for stretchable lithium-ion batteries due to its high specific capacity, robust structural stability, cost-effectiveness, and ease of synthesis. However, its practical application is limited by a low Li^+ diffusion coefficient (10^{-12}–10^{-13} cm^2 s^{-1}) and poor electrical conductivity. To address these challenges, we have developed an innovative yolk-shell V_2O_5 architecture using a facile synthesis method involving spray pyrolysis followed by thermal treatment. This yolk-shell V_2O_5 is coated with a poly(ethylene oxide) (PEO) electrolyte to enhance ion transport contact areas and flexibility. The yolk-shell V_2O_5@PEO is then integrated with a PEO-based polymer electrolyte in a thin film configuration, paired with zig-zag truncated lithium metal anodes for stretchable lithium metal batteries. The integrated film demonstrates superior electrochemical performance due to highly reversible Li^+ insertion/extraction and enhanced Li ion diffusion. The unique design of the stretchable Li-yolk-shell V_2O_5@PEO battery achieves an excellent specific discharge capacity of 261 mAh g^{-1}, compared to 158 mAh g^{-1} for pure V_2O_5 at 0.1C. Additionally, the stretchable Li-yolk-shell V_2O_5@PEO cell exhibits a discharge capacity of 250 mAh g^{-1} under zero-strain conditions and 233.7 mAh g^{-1} under 40 % strain at 0.1C and 40 °C. Characterization through X-ray diffraction (XRD) and scanning electron microscopy (SEM) confirms the nano-sized morphology and high crystallinity of the yolk-shell V_2O_5. X-ray photoelectron spectroscopy (XPS) analysis reveals the transformation of yolk-shell V_2O_5@PEO into α-V_2O_5, ε-$Li_{0.5}V_2O_5$, δ-LiV_2O_5, and γ-$Li_2V_2O_5$ phases during lithium-ion (de)intercalation. This cutting-edge battery design paves the way for the development of high-performance, stretchable, and flexible batteries, ideal for next-generation portable electronic devices.

1. Introduction

The demand for stretchable energy storage configurations is proliferating owing to their applications in wearable electronic devices, such as artificial skin, strain sensors, displays, and light-emitting diodes (LEDs) [1–3]. Lithium-ion batteries (LIBs) are highly suitable for portable stretchable electronic devices because of their long life, high specific energy, and lack of memory effects [4–6]. Stretchable lithium-ion batteries have been developed via structural deformations, such as wrinkled designs, buckled and elastic scaffolds, origami, kirigami, and spiral coil springs [7–12]. However, considering their targeted elasticity, these structure-modified stretchable batteries suffer from various limitations, including low energy density and poor mechanical durability, which compromise their overall stability.

Recently, metal oxides and alloys [13–15] have gained widespread application in energy storage due to their excellent electrochemical properties and high capacity, driving significant advancements in the field. Among these materials, vanadium pentoxide (V_2O_5) stands out as a

* Corresponding authors.
E-mail addresses: fanglin-wu@whut.edu.cn (F. Wu), jscho@chungbuk.ac.kr (J.S. Cho), jaekwang@cju.ac.kr (J.-K. Kim).

https://doi.org/10.1016/j.est.2024.113047
Received 27 April 2024; Received in revised form 30 June 2024; Accepted 18 July 2024

particularly attractive cathode material for stretchable lithium-ion batteries (LIBs). This is due to its high specific capacity, non-toxicity, structural stability, low cost, and ease of synthesis [16]. It delivers a discharge capacity of 147 mAh g^{-1} in the voltage range of 4.0–2.5 V (vs. Li/Li^+) and a high theoretical capacity of 294 mAh g^{-1} for a discharge voltage of 2.0 V corresponding to the transport of one and two lithium ions, respectively [1,17,18]. The reversible Li^+ insertion/extraction in V_2O_5 occurs via the following electrochemical reaction:

$$V_2O_5 + x\ Li^+ + x\ e^- \rightarrow Li_xV_2O_5.$$

However, V_2O_5 has an intrinsically low Li^+ diffusion coefficient (10^{-12}–10^{-13} $cm^2\ S^{-1}$) and electrical conductivity (10^{-2}–10^{-3} S cm^{-1}) [19,20]. limiting its potential utility. Nano shape processing has been proposed as a solution to address the limitations associated with the sluggish kinetic transport leading to the low performance and cycling of LIBs. For example, nanostructured V_2O_5 exhibits enhanced electrochemical performance and sustained capacity stability for energy storage devices [19–26]. Moreover, it provides large electrolyte/electrode contact interfaces by enabling high Li^+ ion flow, which decreases the diffusion distances of lithium-ion kinetic transport and alleviates the structural strain of V_2O_5 upon lithium intercalation/deintercalation during cycling [27,28] (e.g., $LiFePO_4$ [29], $LiCoO_2$ [30], and $LiMn_2O_4$ [31]). Regarding the design of stretchable batteries, introducing point adhesion between the electrode materials, such as employing a spherical morphology between the substrate and electrode, can effectively address the stability limitations during the stretching state of the electrode.

This study modified V_2O_5 to yolk–shell V_2O_5 with a spherical morphology using the spray pyrolysis method followed by heat treatment at a low melting temperature of 700 °C to prepare a stretchable electrode. The yolk–shell V_2O_5 exhibited structural advantages, such as high specific capacity during the first cycle and easier transfer of Li^+ ions [32]. It exhibited improved electrochemical properties at high current densities due to the formation of a large insertion/extraction region and was applied to a stretchable electrode to fabricate a flexible lithium polymer battery. The point adhesion of the yolk–shell V_2O_5 due to the sticky and flexible polymer electrolyte guarantees good adhesion between the electrode material and the current collector, enabling the stretchable LIB to overcome its initially limited mechanical stability [33,34]. For fabricating stretchable lithium metal batteries, the yolk–-shell V_2O_5 was integrated with a poly(ethylene oxide) (PEO)-based stretchable polymer electrolyte by thermocompression into a zig-zag truncated lithium metal electrode. Although the stretchable yolk–shell V_2O_5 and PEO-based polymer electrolyte composite film exhibits low electrochemical performance due to the low conductivity of PEO-based polymer electrolyte (< 10^{-3} mS) at room temperature, it achieves a specific discharge capacity of 250 mAh g^{-1} at 0.1C current density and 40 °C with high stretchability.

2. Experimental

2.1. Synthesis of yolk–shell V_2O_5 powders

Yolk–shell V_2O_5 powders were synthesized following subsequent steps. The synthesis involved spray pyrolysis and heat treatment. First, a precursor solution was prepared by uniformly dispersing 3 g of V_2O_5 in distilled water. Aqueous ammonia was then slowly added to this solution until it became transparent. Subsequently, a red transparent solution was obtained by adding 2 ml of acetic acid. Next, sucrose (30 g) was added until it completely dissolved. The final volume of the solution was increased to 300 ml by adding distilled water. Spray pyrolysis was performed using an ultrasonic spray generator comprising a droplet generator, quartz reactor, and powder collector to obtain a homogenous material. The carrier gas, flow rate, and reactor temperature (process parameters) were N_2, 10 L min^{-1}, and 700 °C, respectively. The subsequent heat treatment involved oxidation at 400 °C for 5 h in air with a heating rate of 5 °C min^{-1}.

2.2. Preparation of PEO-based ternary solid polymer electrolyte

All the processes were conducted in a dry room (dew point < −60 °C at 20 °C). Before the preparation of the cross-linked ternary solid polymer electrolyte, all materials were carefully dried. In particular, PEO (Dow Chemical, WSR 301, Mw = 4,000,000) was pre-dried at 50 °C in vacuum for 48 h with a mechanical pump, followed by further vacuum drying with a turbo molecular pump ($10^{-7}10^{-8}$ mbar) for an additional 48 h. LiTFSI and $PYR_{14}TFSI$ were dried at 150 °C and 110 °C, respectively, under vacuum with a mechanical pump for 20 h and a turbo molecular pump (10^{-7}–10^{-8} mbar) for 48 h. Benzophenone (Aldrich) was dissolved into $PYR_{14}TFSI$ in the ratio of 5 wt% BP/$PYR_{14}TFSI$ and then stirred overnight. The PEO and LiTFSI powders were first mixed in a glass vial, followed by the addition of BP/$PYR_{14}TFSI$ solution to achieve a molar ratio of 10 (PEO): 1 (LiTFSI): 2 ($PYR_{14}TFSI$). The paste-like mixture was sealed under vacuum in a small pouch bag and aged at 100 °C overnight. The homogenous material was sandwiched between two Mylar foils and hot pressed at 100 °C to obtain a thin electrolyte film. Subsequently, this film was crosslinked under UV light using a cube photoirradiator equipped with a 350 W Hg lamp [34.35].

2.3. Preparation of the cathode composite electrode

All processes were conducted in a dry room. The cathode composite film (called V_2O_5@PEO) was prepared by manually mixing the active materials (yolk–shell V_2O_5, 43 wt%), conductive agent (Ketjenblack EC-300, Akzo Nobel, 7 wt%), PEO (Dow Chemical, WSR 301, Mw = 4,000,000, 17.5 wt%), LiTFSI (5 wt%), and $PYR_{14}TFSI$ (27.5 wt%) in a mortar to form a gummy-like mixture, which was then housed in a vacuum-sealed pouch bag. An aging step (100 °C, overnight) was applied to form a homogenous mixture, followed by a sequence hot-pressing step at 100 °C. Finally, a cold calendaring step was used to further reduce the thickness of the composite electrodes to approximately 40 μm. This corresponded to the active material areal loadings ranging from approximately 3.2 mg cm^{-2} [34].

2.4. Material characterization

The morphology of the obtained yolk–shell V_2O_5 powder was investigated using SEM (Philips XL30 SFEG). The quantity of the dopant was assessed using EDS (Philips XL30 SFEG). A FT-IR (Cary670, Main Bench) was used to obtain the IR spectrum by measuring the absorption, penetration, and reflexibility of the indigenous material in the spectral range of 9000–350 cm^{-1}. BET (Micromeritics ASAP 2010) analysis was performed on the surface areas and pores of the powders using N_2 adsorption–desorption isotherms. XPS (Ulvac-PHI PHI Quantera-II) was used to determine the electrochemical state of the material surface using an Al monochromatic X-ray source (1486.6 eV). Micro XRD (Rigaku VariMAX-007HF, Kα radiation = 1.5418 Å) were used to measure the structural components of samples by observing the angle of diffraction by crystals. The amount of coated carbon was determined via elemental analysis using an inductively coupled plasma mass spectrometer (ICP-MS, 7700×).

2.5. Electrochemical testing

The electrochemical performance of V_2O_5@PEO electrode was investigated with a galvanostatic charge–discharge unit (WBCS3000 battery cycler, WonATech, Korea) at 40 °C in the voltage range 4.0–2.0 V at various current densities. CV was performed with a scan rate of 0.2 mV s^{-1} using a heating chamber, WBCS3000 battery cycler, in the potential range 2.0–4.0 V.

3. Results and discussion

The synthesis of yolk–shell V_2O_5 by spray pyrolysis and subsequent heat treatment is shown in Fig. 1. The prepared mixed solvent of V_2O_5 and sucrose was maintained in a quartz reactor at 700 °C and subjected to spray pyrolysis, resulting in the formation of a vanadium oxide (VO_x—C) composite. During this process, V_2O_5 and sucrose experienced phase changes due to polymerization and carbonization. The resulting VO_x-C composite powders then underwent heat treatment at 400 °C in air, initiating combustion. This combustion began at the surface of the powder particles. However, due to the dense structure of the VO_x-C particles and limited oxygen supply to the interior, the combustion did not penetrate deeply, leading to incomplete combustion within the particles. Consequently, a core-shell-structured V_2O_5@VOx-C composite was formed as an intermediate. The outer V_2O_5 shell, created by the combustion of the carbon component, exhibited minimal shrinkage, while the contraction of the VOx-C core during subsequent heating resulted in the formation of a yolk-shell-structured V_2O_5. For the stretchable lithium metal battery, the vapor deposition process was used to inject the PEO polymer electrolyte into the voids of the yolk–shell structure. The injected polymer electrolyte in voids contacted the V_2O_5 core and the effective area for the electrochemical reactions was increased for lithium-ion transfer.

The X-ray diffraction (XRD) pattern of the V_2O_5 powder was used to identify the crystallographic structure between 5° and 45° in the 2θ range (Fig. 2a). All the diffraction peaks were indexed to the orthorhombic V_2O_5 with monoclinic symmetry (space group: *Pmmn*). The lattice parameters were shown as follows: $a = 11.5041$ (Å), $b = 4.3730$ (Å), and $c = 3.5607$ (Å) for a cell volume of V (Å^3) = 179.13. The crystal structure did not exhibit any apparent additional peaks, indicating the absence of impurities. The sharp and strong peaks suggest a high degree of crystallinity [36]. V_2O_5 extended perpendicular to the (010) direction, forming distorted VO_5 square pyramids that extended on both sides of the layers. These layers possessed three distinct crystallographically unequal coordinated O centers. When the V_2O_5 crystals grow along the [010] direction, the area of the [001] surface increases, and the oxygen atoms of the outermost [001] layer tend to form oxygen defects on the crystals, improving the electronic conductivity and electrochemical performance of V_2O_5 [37]. The chemical structure of V_2O_5 is considered as a distorted octahedral VO_6 which serves as the building block of the V_2O_5 crystal structure. The octahedral are erratic in V_2O_5 structure which has five bonding distances of average 1.803 Å and largest bonding 2.80 Å. The distorted VO_6 octahedra from wrapped layers of oxide anions are shared with the near octahedra (Fig. 2b). V_2O_5 structure hosts lithium-ions in tetrahedral sites and that is proper to intercalation and deintercalation of lithium ions in layered structure with as easy separation along (001) lattice plane. The Fourier transform infrared spectrometer (FT-IR) analysis of the yolk-shell V_2O_5 revealed three prominent characteristic absorption bands at approximately 602, 820, and 1012 cm^{-1}, along with a small kink band at 512 cm^{-1} and a broad band at 3595 cm^{-1} (Fig. S1). The bands at 512, 602, and 820 cm^{-1} correspond to the stretching vibrational modes of the V-O-V symmetric stretch and V—O stretching bond. The other band at 1012 cm^{-1} is associated with the vanadyl group (V=O). The band at 3595 cm^{-1} resulted from H–O–H bending or O—H stretching vibrations, indicating the presence of molecular H_2O. These variations provide insights into the yolk–shell V_2O_5 structure [35–43].

Scanning electron microscopy (SEM) characterization with energy-dispersive X-ray spectroscopy (EDS) was used to investigate the morphology of the yolk–shell V_2O_5 powders (Fig. 3). The synthesized yolk–shell V_2O_5 comprised spherical particles like single droplets within the range of 800 nm to 2 μm and were mesoporous with void diameters of approximately 100 nm between the outer and inside spheres (Fig. 3a). The V_2O_5 particles with the special yolk–shell structure exhibited enhanced electrochemical characteristics by expanding the migrating area of lithium ions through the void spaces between the core and the shell (Fig. 3b) [37,41]. Fig. S2 shows the pore size distribution of the shell V_2O_5 according to Brunauer–Emmett–Teller (BET) analysis. The average pore diameter of adsorption was 15.2 nm, and the pores were concentrated at 2 nm. The SEM-EDS analysis confirmed that the PEO-injected yolk–shell V_2O_5 (yolk–shell V_2O_5@PEO) comprised C (red), V (yellow), and O (blue) with a uniform distribution (Fig. 3c–f). The yolk–shell V_2O_5@PEO had fewer pores and a smoother surface than pure yolk-shell V_2O_5 (Fig. 3a and b) because PEO was primarily coated on the surface of the V_2O_5 primary particles to penetrate the void space when the composite V_2O_5@PEO electrode was aged in a vacuum-sealed pouch bag. The cross-sectional micrograph with line-EDS of the yolk–shell V_2O_5@PEO particle is displayed in Fig. S3. The focused ion beam technique was used to estimate the void space and element distribution. Although the void space was not wider than that of pure yolk–shell

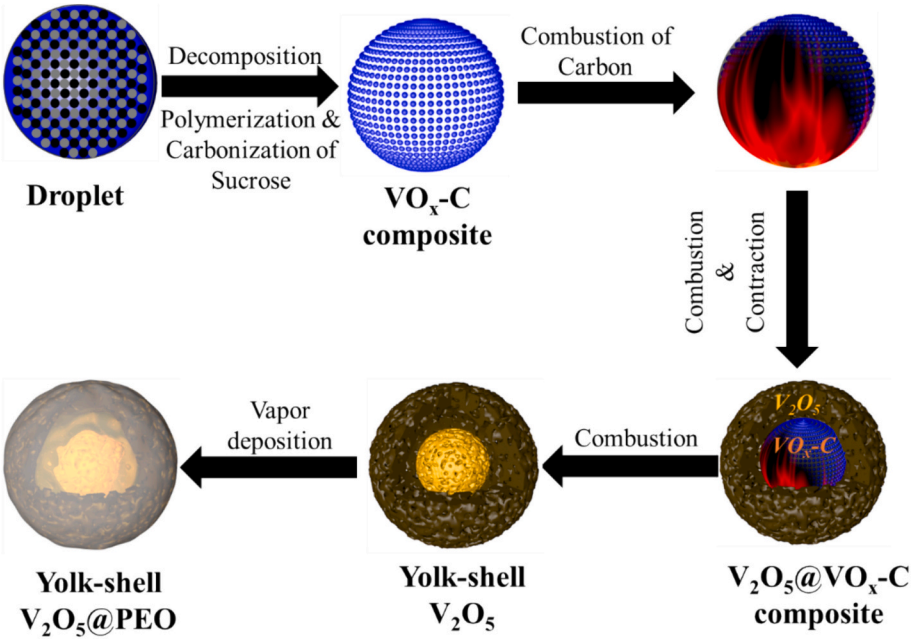

Fig. 1. Schematic of the preparation process of yolk–shell V_2O_5@PEO powder.

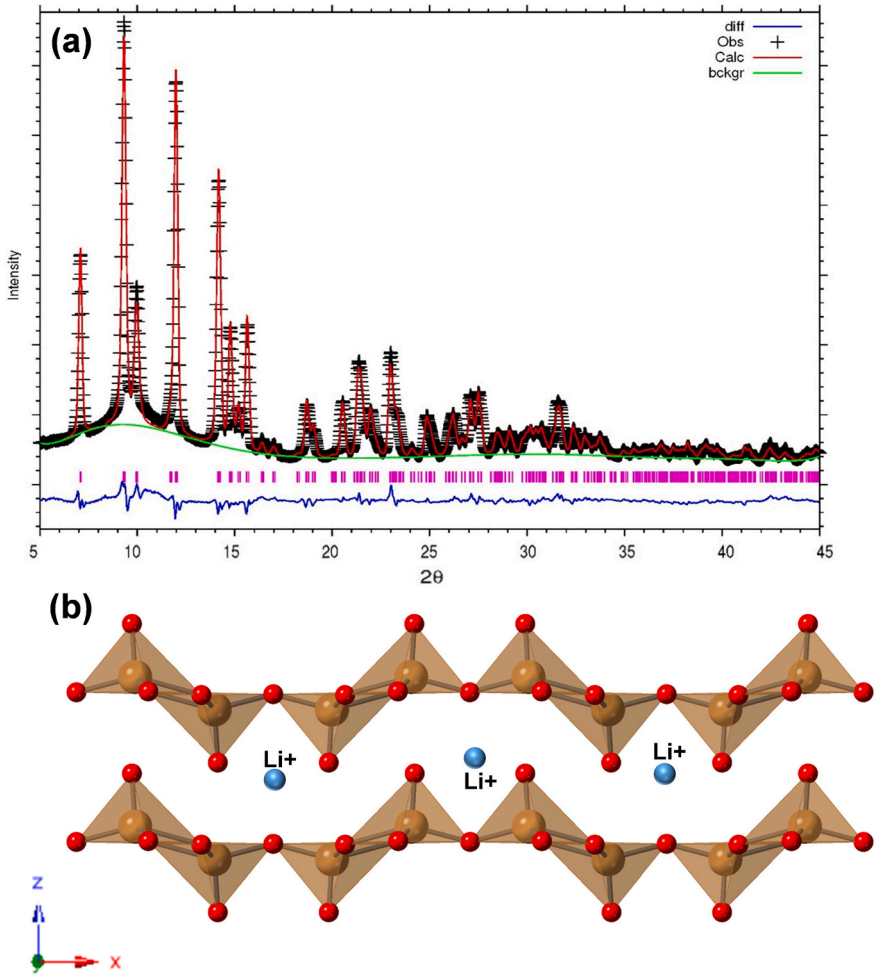

Fig. 2. XRD patterns (a) and crystal structure (b) of yolk-shell V_2O_5.

V_2O_5, it was still formed by a small amount of PEO. V, O, and C were present in all sections of the cutting plane, and the carbon atoms produced by PEO were well distributed along the primary V_2O_5 particles, as well as inside and outside the walls.

The pore structure of the yolk–shell V_2O_5@PEO particles was investigated using TEM (Fig. 4). The yolk–shell V_2O_5@PEO comprised outer and inner spheres, a porous phase formed by the aggregation of primary V_2O_5 particles (Fig. 4a). The yolk-shell structure of the V_2O_5@PEO particles is further illustrated in Fig. S4. The yolk-shell structure is clearly distinguishable from the color contrast observed. Additionally, EDS mapping shows the distribution of elemental O and V, further confirming the yolk-shell structure. In addition, a void was formed between the outer and inner spheres, and a thin PEO layer (~2 nm) was observed on the surface of the V_2O_5 particles (Fig. 4b). The voids prevent the collapse of particles during shrinkage and the expansion of particles during lithiation and delithiation. Moreover, the void and porous structure of the yolk–shell V_2O_5 increased the effective area in contact with the electrolyte and improved the electrochemical performance. In the stretching state, the spherical yolk–shell and void structures enhance the adhesion between the current collector (polymer electrolyte) and the active materials by deformation. The high-resolution TEM image in Fig. 4b shows that the lattice fringe of the primary V_2O_5 particles is visible, with an interplanar spacing of 0.2752 nm, which matches that of the (310) lattice plane of orthorhombic V_2O_5. The TEM-EDS mapping shown in Fig. 4c indicates that the vanadium and carbon atoms are homogeneously distributed along the particle shape, demonstrating that the yolk–shell structure of V_2O_5 was successfully prepared via a simple spray pyrolysis synthesis method without the aggregation of atoms. Moreover, the PEO injected by vapor deposition resided well in the outer and inner spheres. The PEO well coated on all the surfaces benefits the active particles participating in the electrochemical reaction of the stretchable battery.

As cathode in battery, V_2O_5 has three phases (α, δ, γ) within the voltage range of 2–4 V [44]. The fresh-phase V_2O_5 has a layered orthorhombic structure, whereby the VO_5 square pyramids form zig-zag double chains stacked along the [011] direction, sharing edges via weak van der Waals forces. This phase can reversibly insert and extract lithium-ion carriers in vanadium oxides [45,46]. α-V_2O_5 transforms into ε-$Li_{0.5}V_2O_5$ at a discharge potential plateau of 3.22 V [19] according to Eq. (1).

$$\alpha - V_2O_5 + 0.5\ Li^+ + 0.5e^- \leftrightarrow \varepsilon - Li_{0.5}V_2O_5 \quad (1)$$

$$\varepsilon - Li_{0.5}V_2O_5 + 0.5\ Li^+ + 0.5e^- \leftrightarrow \delta - LiV_2O_5 \quad (2)$$

When discharging to 2.5 V, one Li^+ ion is transferred to V^{+4} and V^{+5} at δ-LiV_2O_5 (3.02 V), according to Eq. (2).

$$\delta - LiV_2O_5 + Li^+ + e^- \leftrightarrow \gamma - Li_2V_2O_5 \quad (3)$$

During this process, a structural transfer occurs without the breakage of the strong V—O bonds. This occurs because of the seamless transfer of the VO_5 square pyramids, efficiently transmitting the minimal necessary energy by shifting half a unit cell parameter along the b-axis [44]. Upon discharging to 2.0 V, the γ-$Li_2V_2O_5$ (2.14 V) adsorbs/desorbs two Li ions in V^{+4}, as described by Eq. (3) [46]. This structural deformation is irreversible because it breaks the V—O bonds. A more electrochemical

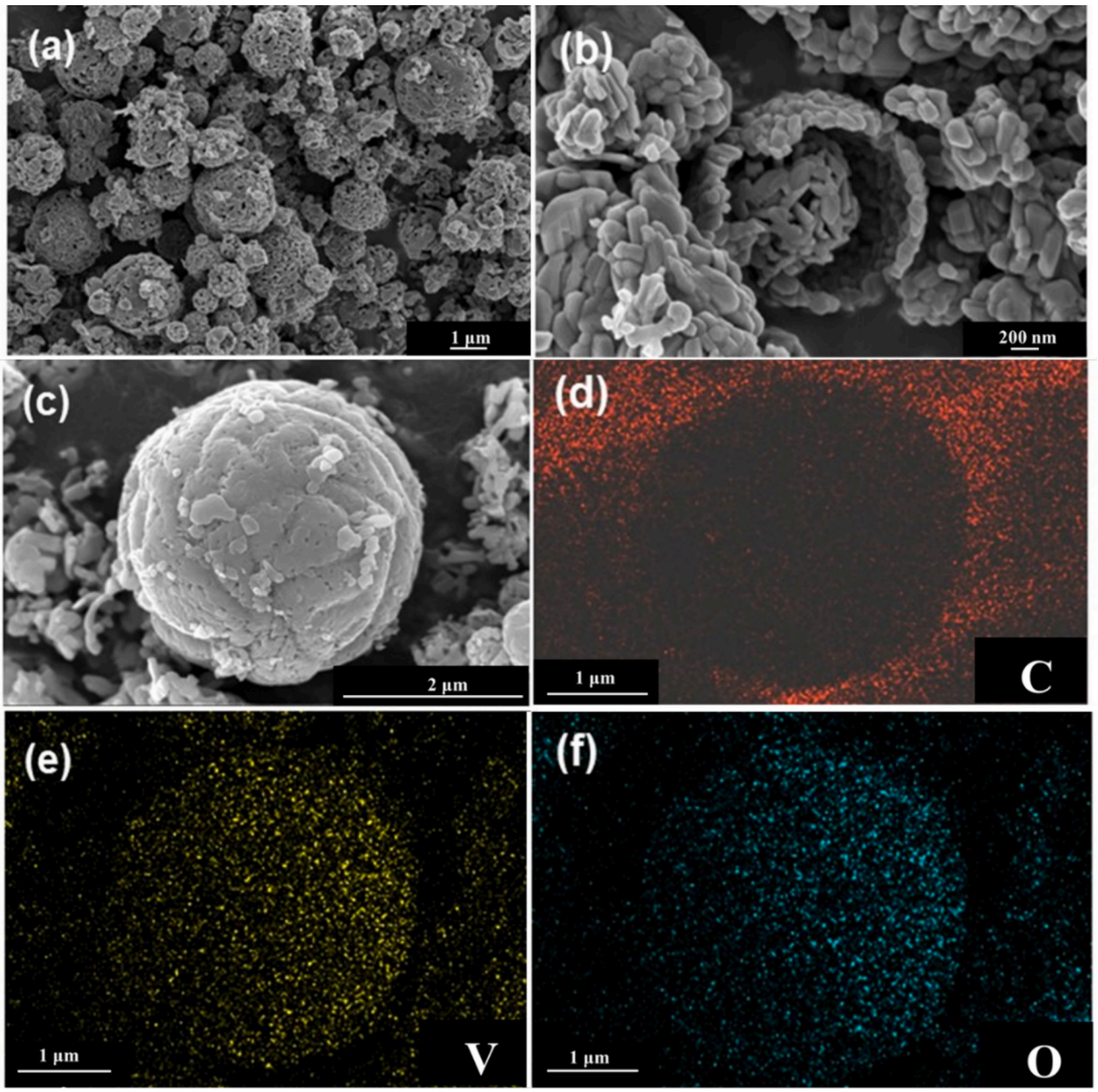

Fig. 3. Scanning electron microscopy (SEM) images of (a) and (b) the yolk–shell structure of V_2O_5 powders and (c) yolk–shell V_2O_5@PEO. Energy-dispersive X-ray spectroscopy (EDS) maps of (d) C, (e) V, and (k) O of the yolk–shell V_2O_5@PEO.

material is obtained by intercalating x-lithium when $0.0 < x < 2$ [44–46]. The practical electrochemical reaction mechanism of the yolk–shell V_2O_5@PEO was investigated using the ex-situ X-ray photoelectron spectrometry (XPS). The ex-situ XPS patterns of the electrodes at different discharge/charge states and 40 °C are shown in Fig. 5. During the lithium-ion insertion process, the XPS peak positions gradually shift toward higher binding energies. The wide-survey XPS profiles of the samples are shown in Fig. S5, which indicate the same predominant signals of V, O, and C. Yolk–shell V_2O_5@PEO was measured under four different voltage plateaus (fresh, discharged to 2.7 V, discharged to 2.0 V, and charged to 4.0 V). The $V2p_{3/2}$ spectrum could be divided into two peaks assigned to V^{4+} and V^{5+}. The peak of the as-prepared yolk–shell V_2O_5@PEO was sharp owing to the appearance of only V^{5+} at 517.8 eV [22,42]. During discharge, the peak was broadened to full discharge to 2.0 V, and V^{4+} and V^{5+} shifted to higher energies because of the lithium-ion interaction. These distinct curves with voltage plateau are associated with the phase transformations of α-V_2O_5 to ε-$Li_{0.5}V_2O_5$, δ-LiV_2O_5, and γ-$Li_2V_2O_5$ [17–19]. The crystal structures were also altered by the lithium-ion intercalation and distortion of the V_2O_5 bonds (Fig. S6) [22]. The first two plateaus at 3.34 and 3.15 V can be ascribed to the phase transition from α-V_2O_5 to ε-$Li_{0.5}V_2O_5$ and δ-LiV_2O_5, respectively. At 2.7 V, the peak balances between V^{4+} and V^{5+} with the formation of δ-LiV_2O_5. The V^{5+} peak continually decreases, while the V^{4+} peak increases at 2.0 V, implying a reduction of V_2O_5 at the γ-$Li_2V_2O_5$ phase. A few V^{5+} peaks remain because not all the V_2O_5 participate in the reduction reaction, resulting in a lower discharge capacity than the theoretical capacity. In the charged yolk–shell V_2O_5@PEO, the V^{4+} peak disappears at 517.1 eV, accompanying the recovered peak of V^{5+}, which is consistent with the redox reaction of yolk–shell V_2O_5@PEO.

To investigate the electrochemical performance of the yolk–shell structure V_2O_5, Fig. 6a compares the charge–discharge curves of

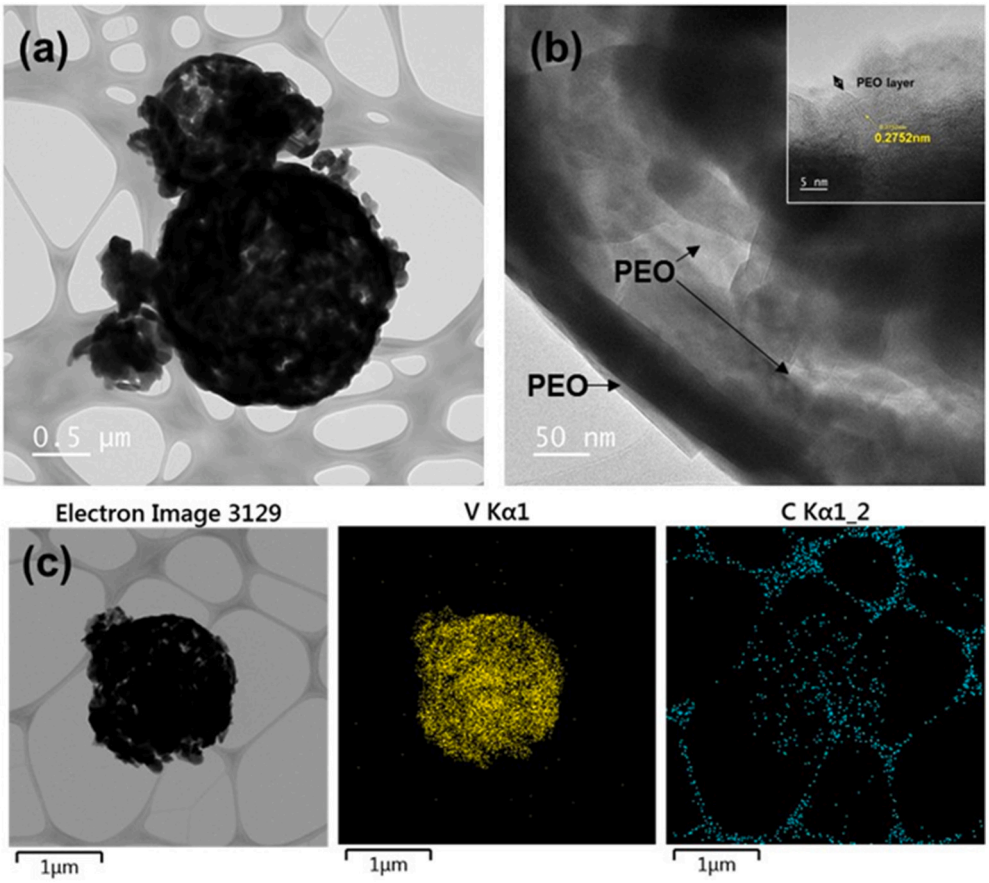

Fig. 4. TEM (a, b) and TEM-EDS (c) images of yolk–shell V_2O_5@PEO powders.

conventional bare V_2O_5@PEO and yolk–shell V_2O_5@PEO in stretchable lithium metal batteries. The initial charge–discharge curves for the yolk–shell V_2O_5@PEO cells at 0.1, 0.2, 0.5, and 1C rate test cycles at 40 °C, when the voltage range is set at 2.0–4.0 V, are shown in Fig. 6b. The discharge capacities were 261, 234.7, 200.2, and 179.6 mAh g^{-1} for the respective current densities. As the current density decreased, the initial discharge specific capacity increased. The initial capacity at 0.1C was close to the theoretical capacity of V_2O_5 (294 mAh g^{-1}), and the yolk–shell V_2O_5@PEO delivered a higher capacity than the purchased V_2O_5 prepared by the conventional method. Moreover, several clear voltage plateaus were observed during the lithium insertion process at approximately 3.2, 2.3, and 2.1 V (vs. Li/Li^+) in the first discharge curve for yolk–shell V_2O_5@PEO. Apparent differences in capacity were observed between the conventional bare V_2O_5@PEO and yolk–shell V_2O_5@PEO (Fig. 6a). Conventional V_2O_5@PEO cell exhibited an initial discharge capacity of approximately 158 mAh g^{-1}, whereas the initial discharge capacity of yolk–shell V_2O_5@PEO cell was approximately 261 mAh g^{-1}. This suggests that the Li^+ ion diffusion was facilitated by decreasing the diffusion length by passing the electrolyte through the void space created by the core and shell structures of the yolk–shell V_2O_5@PEO. V_2O_5@PEO can be attributed to the plateaus at approximately 3.30, 3.05, and 2.07 V, whereas the yolk–shell V_2O_5@PEO can be attributed to the plateaus at around 3.33, 3.14, and 2.24 V. The curve shape evolved according to the crystals in the material, and the yolk–-shell V_2O_5 exhibited excellent structural stability without any undesired reactions. Fig. S7 shows the cyclic voltammetry (CV) results of the Li/yolk–shell V_2O_5@PEO stretchable cell for the first and second cycles scanned at 0.2 mV s^{-1} and 40 °C. Three reversible peaks were observed in accordance with the Li-ion intercalation reaction. The cathodic peaks related to the phase transformation were observed at 3.22, 3.02, and 2.14 V (vs. Li/Li^+). Two peaks were observed at 3.0–4.0 V, which primarily indicate the phase transformation from crystalline α-V_2O_5 to ε-$Li_{0.5}V_2O_5$ and δ-LiV_2O_5 by the insertion of 0.5 Li^+. The remaining peaks indicate the phase transformation from δ-LiV_2O_5 to γ-$Li_2V_2O_5$ by the insertion of one Li^+ [40,43]. These phase transformations typically match the plateaus observed in Fig. 5. Fig. 6c shows the rate performances of the conventional bare V_2O_5@PEO and yolk–shell V_2O_5@PEO at various current rates (0.1, 0.2, 0.5, and 1C). Although the storage capacities of the two samples were stable at all current densities, the yolk–shell V_2O_5@PEO cells showed a higher capacity at all current densities, and the difference in capacity increased at a high current density of 1C. Furthermore, the capacity recovery of yolk–shell V_2O_5@PEO cell was 98.8 % when the current density reverted back to 0.1C from 1C (conventional V_2O_5 is 87.2 %). This high recovery can be ascribed to its superior rate capability and stable crystal structure.

An integrated film composed of an electrode and polymer electrolyte was prepared by hot-press calendaring after blending the integrated electrode and polymer electrolyte. The integrated film exhibited high stretchability (Fig. 7a). Many grape-like clusters were distributed on the electrode side of the integrated film because of the high concentration of concentrated yolk–shell V_2O_5@PEO (Fig. S8). Polymer chains and carbon black were homogeneously distributed among the particles. Considering the polymer electrolyte side of the integrated film, although the wrinkles on the polymer film were visible, its surface was significantly different from that of the electrode side. However, the V atom, observed by SEM-EDS, indicated the thinness of the polymer electrolyte (Fig. S9). The ionic conductivity of the polymer electrolyte (PE, PEO/LiTFSI/PYR14TFSI) was evaluated and is shown in Fig. S10. Impressively, the polymer electrolyte demonstrated an ionic conductivity of 0.97×10^{-3} S cm^{-1} at 30 °C, highlighting its robust electrochemical performance. The interfacial stability and polarization voltage were also assessed using a symmetric Li|PE|Li battery configuration with direct

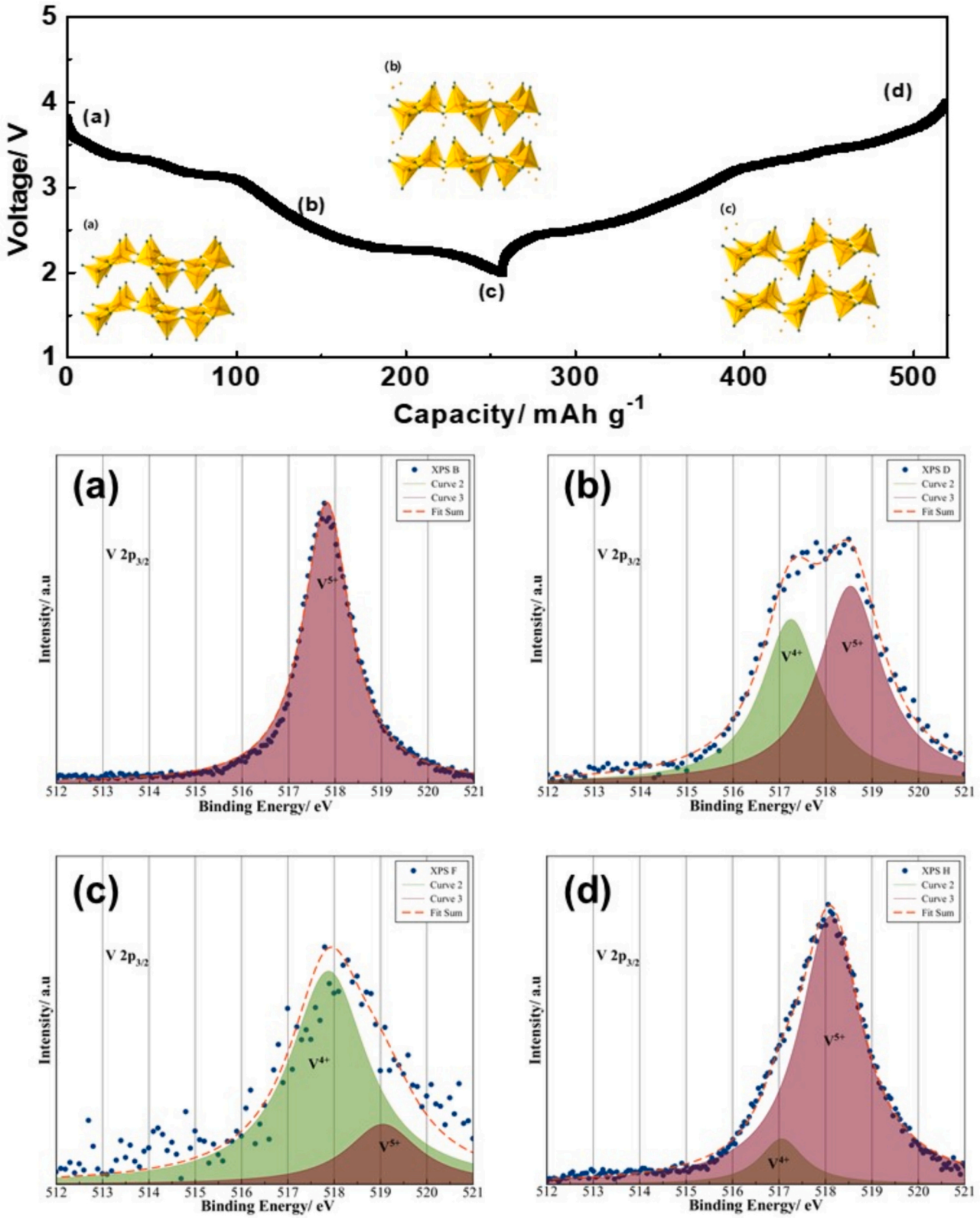

Fig. 5. (a) Galvanostatic discharge–charge curve of yolk–shell V_2O_5@PEO at a rate of 0.1C. (b) Ex-situ XPS spectra of yolk–shell V_2O_5@PEO at each voltage state during cycling. XPS elemental scans of V2p3 core peaks: (a) pristine phase, (b) after discharging to 2.7 V, (c) after discharging to 2.0 V, and (d) after charging to 4.0 V.

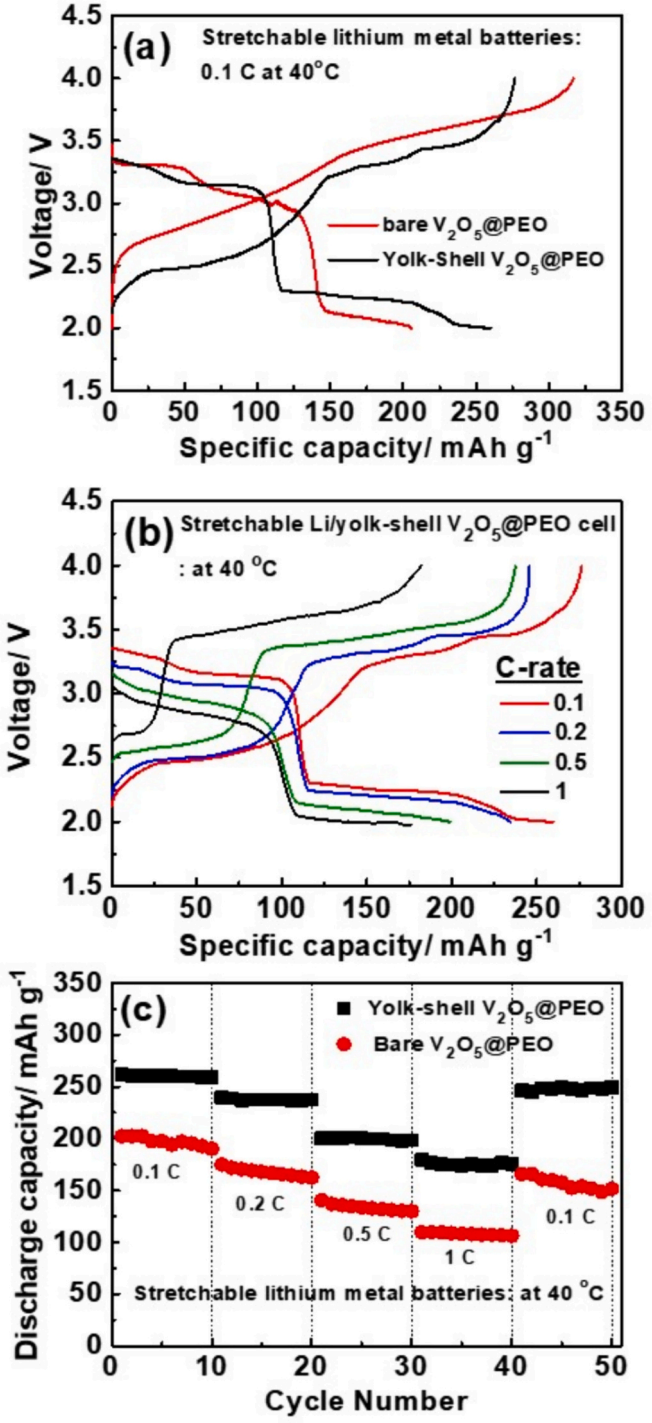

Fig. 6. (a) Electrochemical performances of conventional bare V_2O_5@PEO and yolk–shell V_2O_5@PEO cells at 0.1C for 40 °C. (b) Initial charge–discharge curves of the yolk–shell V_2O_5@PEO cells at different current densities in the voltage range 4.0–2.0 V. (c) C-rate performance of conventional V_2O_5@PEO and yolk–shell V_2O_5@PEO cells at various current rates (0.1C, 0.2C, 0.5C, and 1C at 40 °C).

current at room temperature. As depicted in Fig. S11, the Li|PE|Li symmetric battery exhibited a remarkably low polarization voltage and maintained flat, stable voltage plateaus for 300 h. This consistency indicates uniform electroplating/stripping of Li with minimal fluctuations, demonstrating the outstanding stability and reliable performance of the polymer electrolyte during prolonged operation.

Anodes of stretchable batteries also require stretchability; lithium metal is emerging as a promising anode for lithium-ion batteries owing to its high specific energy and low negative electrochemical potential [47]. However, V_2O_5, which is not a lithium source, has to be applied with a lithium metal anode. Although using lithium metal electrodes as stretchable electrodes is challenging, zigzag-truncating architectures are favorable for application in stretchable electrodes (Fig. 7b). The stretchable lithium metal battery comprised an integrated film, zigzag-truncated lithium metal, and polydimethylsiloxane (PDMS) packing (Fig. 7c). A dimethyl sulfoxide doped PEDOT:PSS polymer substrate was used as the stretchable current collector. The manufacturing process of the stretchable lithium metal battery is shown in Fig. S12. For the final cell, the components were laminated and pressed at 1 MPa. Fig. 7d shows the charge–discharge curves of the Li/yolk–shell V_2O_5@PEO stretchable cell at a rate of 0.1C and 40 °C with 20 % stretching. The initial discharge curve of the cell presented three voltage plateaus at 3.26, 3.06, and 2.21 V, and 1.67 Li^+ (245 mAh g^{-1}) was inserted into the cathode. The stretched-state cell exhibited a higher voltage difference between the discharge and charge curves because of its increased resistance to tensile stress. The appearance of the discharge curves was almost identical during the five cycles. There were three oxidation voltages located at approximately 2.54, 3.3, and 3.52 V corresponding to the reduction voltages, suggesting good reversibility of the electrochemical reaction with useful contact between injected PEO polymer electrolyte and primary V_2O_5 particles in the stretching state [48]. Fig. 7e shows the cycling properties of Li/yolk–shell V_2O_5@PEO stretchable cells at 0 % and 20 % stretching. The flatness-state cell (0 % stretching) demonstrated stable cycling performance over 100 cycles with 98.8 % capacity retention. However, the 20 % stretching cell initially showed a first discharge capacity of up to 245.0 mAh g^{-1} during the first five cycles, but the discharge capacity rapidly decreased by the 60th cycle due to tensile stress. Additionally, the flatness-state cell (0 % stretching) with excellent reversible capacity and a long lifespan is shown in Fig. S13. The EIS results (Fig. S14) suggest that the bulk electrolyte resistance and interfacial and charging transfer resistances significantly increased after 100 cycles in the 20 % stretching state. The initial adhesion strength of integrated electrode was excellent, but it appeared to be loosened by continuous tension at 20 % stretching. Nevertheless, the reversible discharge capacity was still high at 176.6 mAh g^{-1} after 100 cycles with 70.6 % capacity retention, which shows that the integrated electrode and zig-zag truncated lithium metal could be a good electrode concept for stretchable lithium metal batteries. However, optimization of the process and materials in the concept is required for a stable long life in the stretching state. Fig. 7f shows the performance of the stretchable Li/yolk–shell V_2O_5@PEO metal battery in various stretching states. The discharge capacity was maintained at 245.2 and 233.7 mAh g^{-1} at 20 % and 40 % stretching states even after five cycles of bending, compared to 250 mAh g^{-1} before stretching. The capacities slightly decreased to 2 % and 7 % at 20 % and 40 % stretching, respectively, but the capacity at 40 % stretching decreased to 225.1 mAh g^{-1} during the five cycles. Their capacities significantly recovered to 248.3 mAh g^{-1} when the stretchable cell was back to 0 % stretching. The capacity of the stretchable Li/yolk–shell V_2O_5@PEO metal battery did not decrease significantly even after stretching. Optical images of the stretchable lithium metal battery connected to a red LED are shown in Fig. S15. The stretchable lithium metal battery continuously powered the LED after stretching 10 times to a 40 % stretching state. The excellent electrochemical results of the stretchable Li/yolk–shell V_2O_5@PEO metal battery are attributed to the large area of contact between the primary V_2O_5 particles and the polymer electrolyte, good point adhesion in the integrated electrode, short movement path of ions, and unique stretchable lithium metal electrode architecture.

4. Conclusion

Yolk–shell V_2O_5@PEO powders were successfully prepared by a facile route combining spray pyrolysis, subsequent heat treatment, and

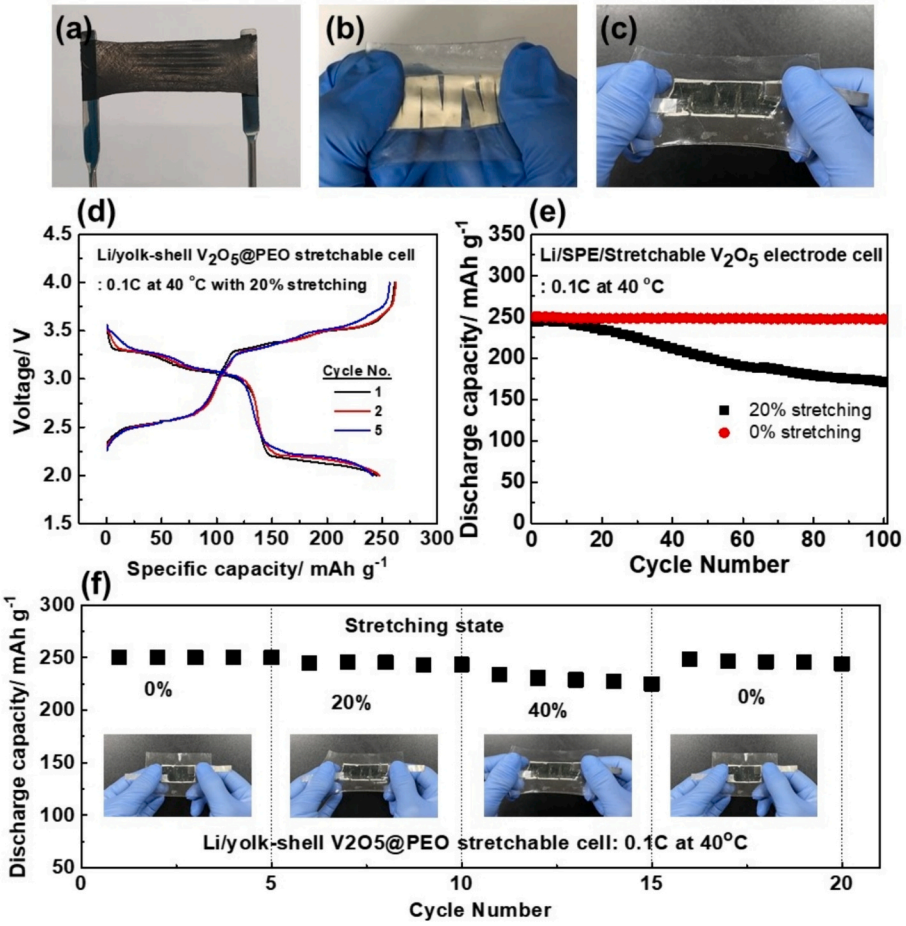

Fig. 7. Images of the integrated V_2O_5@PEO film (a), zig-zag truncating lithium metal (b), and stretchable Li/yolk–shell V_2O_5@PEO metal battery (c). Charge–discharge curves (d) and cycle performance (e) of the stretchable Li/yolk–shell V_2O_5@PEO metal battery at 0.1C for 40 °C. Short-cycle performance (f) of the stretchable Li/yolk–shell V_2O_5@PEO metal battery in several stretching states.

vapor deposition. The yolk–shell V_2O_5@PEO integrated electrode film was employed as the positive electrode with a PEO-based polymer electrolyte in a stretchable lithium metal battery. The yolk–shell V_2O_5@PEO powders comprised an unusual core–void–shell structure with increased charge–discharge capacities and superior rate capabilities than those of conventional V_2O_5. The yolk-shell V_2O_5@PEO is integrated with a PEO-based polymer electrolyte in a thin film. The stretchable lithium metal battery using a zig-zag truncated lithium metal anode showed excellent electrochemical performance, such as a high discharge capacity of 250 mAh g^{-1} at 0.1C for 40 °C and high stretchability with 93 % capacity retention in 40 % stretching state. The PEO-filled voids formed by this distinctive structure facilitate the diffusion of Li ions by reducing the diffusion length and enabling free electrolyte penetration. The yolk–shell V_2O_5@PEO demonstrated robust adhesion, and the integrated electrode exhibited good contact with flexibility in the stretching state. The zig-zag truncated electrode design can enable the application of metal electrodes in stretchable batteries, making this specially designed stretchable battery suitable for diverse practical applications.

CRediT authorship contribution statement

Muthu Gnana Theresa Nathan: Writing – original draft, Formal analysis, Data curation. **Seon-Young Yeon:** Writing – original draft, Investigation, Data curation, Conceptualization. **Jae Seob Lee:** Methodology, Investigation. **Min Su Jo:** Investigation. **Gil Chan Hwang:** Software, Methodology. **Hong-Il Kim:** Project administration, Methodology. **Fanglin Wu:** Writing – review & editing, Validation. **Guk-Tae Kim:** Validation, Methodology, Formal analysis. **Ying Liu:** Methodology, Writing – review & editing. **Jin-Hee Kim:** Visualization, Project administration, Funding acquisition. **Jung Sang Cho:** Writing – review & editing, Supervision, Methodology. **Jae-Kwang Kim:** Writing – review & editing, Validation, Supervision, Data curation, Conceptualization.

Declaration of competing interest

The authors declare that they have no known competing financial interests or personal relationships that could have appeared to influence the work reported in this paper.

Data availability

No data was used for the research described in the article.

Acknowledgements

M. G. T. N. and S.-Y. Y. contributed equally to this work. This work was supported by the National Research Foundation of Korea (NRF) grants funded by the Korean government (MSIT) (RS-2023-00248824, 2019R1I1A3A01050978 and RS-2023-00217581).

Appendix A. Supplementary data

Supplementary data to this article can be found online at https://doi.org/10.1016/j.est.2024.113047.

References

[1] M. Amjadi, K.U. Kyung, I. Park, M. Sitti, Stretchable, skin-mountable, and wearable strain sensors and their potential applications: a review, Adv. Funct. Mater. 26 (2016) 1678–1698, https://doi.org/10.1002/adfm.201504755.

[2] S. Choi, H. Lee, R. Ghaffari, T. Hyeon, D.H. Kim, Recent advances in flexible and stretchable bio-electronic devices integrated with nanomaterials, Adv. Mater. 28 (2016) 4203–4218, https://doi.org/10.1002/adma.201504150.

[3] T.Q. Trung, N.E. Lee, Recent progress on stretchable electronic devices with intrinsically stretchable components, Adv. Mater. 29 (2017) 1603167, https://doi.org/10.1002/adma.201603167.

[4] X. Feng, M. Ouyang, X. Liu, L. Lu, Y. Xia, X. He, Thermal runaway mechanism of lithium ion battery for electric vehicles: a review, Energy Storage Mater. 10 (2018) 246–267, https://doi.org/10.1016/j.ensm.2017.05.013.

[5] F. Wu, J. Maier, Y. Yu, Guidelines and trends for next-generation rechargeable lithium and lithium-ion batteries, Chem. Soc. Rev. 49 (2020) 1569–1614, https://doi.org/10.1039/C7CS00863E.

[6] F. Wu, Z. Chen, S. Fang, W. Zuo, G.T. Kim, S. Passerini, The role of ionic liquids in resolving the interfacial chemistry for (quasi-) solid-state batteries, Energy Storage Mater. 63 (2023) 103062, https://doi.org/10.1016/j.ensm.2023.103062.

[7] O.H. Kwon, J. Ryu, J.H. Lee, H.W. Kim, J.S. Cho, S.M. Jeong, D.W. Kang, J.K. Kim, Stretchable self-charging energy integrated device of high storage efficiency, J. Power Sources 525 (2022) 231079, https://doi.org/10.1016/j.jpowsour.

[8] C. Wang, W. Zheng, Z. Yue, C.O. Too, G.G. Wallace, Buckled, stretchable polypyrrole electrodes for battery applications, Adv. Mater. 23 (2011) 3580–3584, https://doi.org/10.1002/adma.201101067.

[9] W. Liu, J. Chen, Z. Chen, K. Liu, G. Zhou, Y. Sun, M.S. Song, Z. Bao, Y. Cui, Stretchable lithium-ion batteries enabled by device-scaled wavy structure and elastic-sticky separator, Adv. Energy Mater. 7 (2017) 1701076, https://doi.org/10.1002/aenm.201701076.

[10] Z. Song, T. Ma, R. Tang, Q. Cheng, X. Wang, D. Krishnaraju, R. Panat, C. Chan, H. Yu, H. Jiang, Origami lithium-ion batteries, Nat. Commun. 5 (2014) 3140, https://doi.org/10.1038/ncomms4140.

[11] Z. Song, X. Wang, C. Lv, Y. An, M. Liang, T. Ma, D. He, Y.J. Zheng, S.Q. Huang, H. Yu, H. Jiang, Kirigami-based stretchable lithium-ion batteries, Sci. Rep. 5 (2015) 10988, https://doi.org/10.1038/srep10988.

[12] J. Ren, Y. Zhang, W. Bai, X. Chen, Z. Zhang, X. Fang, W. Weng, Y. Wang, H. Peng, Elastic and wearable wire-shaped lithium-ion battery with high electrochemical performance, Angew. Chem. Int. Ed. 126 (2014) 7998–8003, https://doi.org/10.1002/ange.201402388.

[13] J. Wang, F. Zheng, M. Li, J. Wang, D. Jia, X. Mao, P. Hu, Q. Zhen, Y. Yu, V_2O_5@RuO_2 core-shell heterojunction nano-arrays as electrode material for supercapacitors, Chem. Eng. J. 446 (2022) 136922, https://doi.org/10.1016/j.cej.2022.136922.

[14] M. Tian, R. Li, C. Liu, D. Long, G. Cao, An aqueous Al-ion supercapacitor with V_2O_5 mesoporous carbon electrodes, ACS Appl. Mater. Interfaces 11 (2019) 15573–15580, https://doi.org/10.1021/acsami.9b02030.

[15] Y. Zhang, B. Chen, Y. Qiao, Y. Duan, X. Qi, S. He, H. Zhou, J. Chen, A. Yuan, S. Zheng, FeNi alloys incorporated N-doped carbon nanotubes as efficient bifunctional electrocatalyst with phase-dependent activity for oxygen and hydrogen evolution reactions, J. Mater. Sci. Technol. 201 (2024) 157–165, https://doi.org/10.1016/j.jmst.2024.03.046.

[16] R. Sasikumar, M. Govindasamy, S.M. Chen, Y. Chieh-Liu, P. Ranganathan, S. P. Rwei, Electrochemical determination of morin in kiwi and strawberry fruit samples using vanadium pentoxide nano-flake, J. Colloid Interface Sci. 504 (2017) 626–632, https://doi.org/10.1016/j.jcis.2017.03.039.

[17] T. Zhai, H. Liu, H. Li, X. Fang, M. Liao, L. Li, H. Zhou, Y. Koide, Y. Bando, D. Golberg, Centimeter-long V_2O_5 nanowires: from synthesis to field-emission, electrochemical, electrical transport, and photoconductive properties, Adv. Mater. 22 (2010) 2547–2552, https://doi.org/10.1002/adma.200903586.

[18] S. Liang, Y. Hu, Z. Nie, H. Huang, T. Chen, A. Pana, G. Cao, Template-free synthesis of ultra-large V_2O_5 nanosheets with exceptional small thickness for high-performance lithium-ion batteries, Nano Energy 13 (2015) 58–66, https://doi.org/10.1016/j.nanoen.2015.01.049.

[19] J.M. Cocciantelli, J.P. Doumerc, M. Pouchard, M. Broussely, J. Labat, Crystal chemistry of electrochemically inserted $Li_xV_2O_5$, J. Power Sources 34 (1991) 103–111, https://doi.org/10.1016/0378-7753(91)85029-V.

[20] C. Delmas, H. Cognac-Auradou, J.M. Cocciantelli, M. Menetrier, J.P. Doumerc, The $Li_xV_2O_5$ system: An overview of the structure modifications induced by the lithium intercalation, Solid State Ionics 69 (1994) 257–264, https://doi.org/10.1016/0167-2738(94)90414-6.

[21] Y.L. Cheah, V. Aravindan, S. Madhavi, Chemical lithiation studies on combustion synthesized V_2O_5 cathodes with full cell application for lithium ion batteries, J. Electrochem. Soc. 160 (2013), https://doi.org/10.1149/2.015308jes. A1016.

[22] C.F. Armer, M. Lübke, M.V. Reddy, J.A. Darr, X. Li, A. Lowe, Phase change effect on the structural and electrochemical behaviour of pure and doped vanadium pentoxide as positive electrodes for lithium ion batteries, J. Power Sources 353 (2017) 40–50, https://doi.org/10.1016/j.jpowsour.2017.03.121.

[23] A. Pan, J.G. Zhang, Z. Nie, G. Cao, B.W. Arey, G. Li, S.Q. Liang, J. Liu, Facile synthesized nanorod structured vanadium pentoxide for high-rate lithium batteries, J. Mater. Chem. 20 (2010) 9193–9199, https://doi.org/10.1039/C0JM01306D.

[24] Y. Wang, K. Takahashi, K. Lee, G. Cao, Nanostructured vanadium oxide electrodes for enhanced lithium-ion intercalation, Adv. Funct. Mater. 16 (2006) 1133–1144, https://doi.org/10.1002/adfm.200500662.

[25] J.W. Lee, S.Y. Lim, H.M. Jeong, T.H. Hwang, J.K. Kang, J.W. Choi, Extremely stable cycling of ultra-thin V_2O_5 nanowire–graphene electrodes for lithium rechargeable battery cathodes, Energ, Environ. Sci. 5 (2012) 9889–9894, https://doi.org/10.1039/C2EE22004K.

[26] D. Kong, X. Li, Y. Zhang, X. Hai, B. Wang, X. Qiu, Q. Song, Q.-H. Yang, L. Zhi, Encapsulating V_2O_5 into carbon nanotubes enables the synthesis of flexible high-performance lithium ion batteries, Energ, Environ. Sci. 9 (2016) 906–911, https://doi.org/10.1039/C5EE03345D.

[27] H.T. Tan, X. Rui, W. Sun, G. Yan, T.M. Lim, Vanadium-based nanostructure materials for secondary lithium battery applications, Nanoscale 7 (2015) 14595–14607, https://doi.org/10.1039/C5NR04126K.

[28] L. Mai, Q. Wei, X. Tian, Y. Zhao, Q. An, Electrochemical nanowire devices for energy storage, IEEE T. Nanotechnol. 13 (2013) 10–15, https://doi.org/10.1109/TNANO.2013.2276524.

[29] S. Kraas, A. Vijn, M. Falk, B. Ufer, B. Luerßen, J. Janek, M. Fröba, Nanostructured and nanoporous $LiFePO_4$ and $LiNi_{0.5}Mn_{1.5}O_{4-\delta}$ as cathode materials for lithium-ion batteries, Prog. Solid State Ch. 42 (2014) 218–241.

[30] M. Okubo, E. Hosono, J. Kim, M. Enomoto, N. Kojima, T. Kudo, H. Zhou, I. Honma, Nanosize effect on high-rate Li-ion intercalation in $LiCoO_2$ electrode, J. Am. Chem. Soc. 129 (2007) 7444–7452, https://doi.org/10.1021/ja0681927.

[31] M. Okubo, Y. Mizuno, H. Yamada, J. Kim, E. Hosono, H. Zhou, T. Kudo, I. Honma, Fast Li-ion insertion into nanosized $LiMn_2O_4$ without domain boundaries, ACS Nano 4 (2010) 741–752, https://doi.org/10.1021/nn9012065.

[32] Y.N. Ko, Y.C. Kang, S.B. Park, A new strategy for synthesizing yolk–shell V_2O_5 powders with low melting temperature for high performance Li-ion batteries, Nanoscale 5 (2013) 8899–8903, https://doi.org/10.1039/C3NR02625F.

[33] M. Gu, W.-J. Song, J. Hong, S.Y. Kim, T.J. Shin, N.A. Kotov, S. Park, B.S. Kim, Stretchable batteries with gradient multilayer conductors, Sci. Adv. 5 (2019) eaaw1879, https://doi.org/10.1126/sciadv.aaw1879.

[34] M. Wetjen, G.T. Kim, M. Joost, G.B. Appetecchi, M. Winter, S. Passerini, Thermal and electrochemical properties of PEO-LiTFSI-Pyr_{14}TFSI-based composite cathodes, incorporating 4V-class cathode active materials, J. Power Sources 246 (2014) 846–857, https://doi.org/10.1016/j.jpowsour.2013.08.037.

[35] F. Wu, S. Fang, M. Kuenzel, T. Diemant, J.K. Kim, D. Bresser, G.T. Kim, S. Passerini, Bilayer solid electrolyte enabling quasi-solid-state lithium-metal batteries, J. Power Sources 557 (2013) 232514, https://doi.org/10.1016/j.jpowsour.2022.232514.

[36] Y.S. Hu, X. Liu, J.O. Muller, R. Schlogl, J. Maier, D.S. Su, Synthesis and electrode performance of nanostructured V_2O_5 by using a carbon tube-in-tube as a nanoreactor and an efficient mixed-conducting network, Angew. Chem. Int. Ed. 48 (2009) 210–214, https://doi.org/10.1002/anie.200802988.

[37] C.R. Fell, D. Qian, K.J. Carroll, M. Chi, J.L. Jones, Y.S. Meng, Correlation between oxygen vacancy, microstrain, and cation distribution in lithium-excess layered oxides during the first electrochemical cycle, Chem. Mater. 25 (2013) 1621–1629, https://doi.org/10.1021/cm4000119.

[38] S.Z. Huang, Y. Cai, J. Jin, Y. Li, X.F. Zheng, H.E. Wang, M. Wu, L.H. Chen, B.L. Su, Annealed vanadium oxide nanowires and nanotubes as high performance cathode materials for lithium ion batteries, J. Mater. Chem. A 2 (2014) 14099–14108, https://doi.org/10.1039/C4TA02339K.

[39] N. Kerkouri, M. Haddad, M. Et-tabirou, A. Chahine, L. Laanab, FTIR, Raman, EPR and optical absorption spectral studies on V_2O_5-doped cadmium phosphate glasses, Physica B 406 (2011) 3142–3148, https://doi.org/10.1016/j.physb.2011.04.057.

[40] C. O'Dwyer, V. Lavayen, S.B. Newcomb, M.A. Santa Ana, E. Benavente, G. Gonzalez, C.M. Sotomayor Torres, Vanadate conformation variations in vanadium pentoxide nanostructures, J. Electrochem. Soc. 154 (2007) K29, https://doi.org/10.1149/1.2746556.

[41] X.W. Lou, L.A. Archer, Z. Yang, Hollow micro−/nanostructures: synthesis and applications, Adv. Mater. 20 (2008) 3987–4019, https://doi.org/10.1002/adma.200800854.

[42] J.S. Han, G.C. Hwang, H. Yu, D.H. Lim, J.S. Cho, M. Kuenzeld, J.K. Kim, J.H. Ahn, Preparation of fully flexible lithium metal batteries with free-standing β-$Na_{0.33}V_2O_5$ cathodes and LAGP hybrid solid electrolytes, J. Ind. Eng. Chem. 94 (2021) 368–375, https://doi.org/10.1016/j.jiec.2020.11.011.

[43] M. Gotic, S. Popovie, M. Ivanda, S. Music, Sol–gel synthesis and characterization of V_2O_5 powders, Mater. Lett. 57 (2003) 3186–3192, https://doi.org/10.1016/S0167-577X(03)00022-3.

[44] D. Chao, X. Xia, J. Liu, Z. Fan, C.F. Ng, J. Lin, H. Zhan, Z.X. Shen, H.J. Fan, A V_2O_5/conductive-polymer core/shell nanobelt array on three-dimensional graphite foam: a high-rate, ultrastable, and freestanding cathode for lithium-ion batteries, Adv. Mater. 26 (2014) 5794–5800, https://doi.org/10.1002/adma.201400719.

[45] D. McNulty, D.N. Buckley, C. O'Dwyer, Synthesis and electrochemical properties of vanadium oxide materials and structures as Li-ion battery positive electrodes, J. Power Sources 267 (2014) 831–873, https://doi.org/10.1016/j.jpowsour.2014.05.115.

[46] T. Zhai, H. Liu, H. Li, X. Fang, M. Liao, L. Li, H. Zhou, Y. Koide, Y. Bando, D. Golberg, Centimeter-long V_2O_5 nanowires: from synthesis to field-emission,

electrochemical, electrical transport, and photoconductive properties, Adv. Mater. 22 (2010) 2547–2552, https://doi.org/10.1002/adma.200903586.
[47] S. Fang, F. Wu, S. Zhao, M. Zarrabeitia, G.T. Kim, J.K. Kim, N. Zhou, S. Passerini, Adaptive multi-site gradient adsorption of siloxane-based protective layers enable high performance lithium-metal batteries, Adv. Energy Mater. 13 (2023) 2302577, https://doi.org/10.1002/aenm.202302577.
[48] J. Mohanta, D.W. Kang, J.S. Cho, S.M. Jeong, J.K. Kim, Stretchable electrolytes for stretchable/flexible energy storage systems–recent developments, Energy Storage Mater. 28 (2020) 315–324, https://doi.org/10.1016/j.ensm.2020.03.009.